Full length article

Atomic-scale characterization of subsurface damage and structural changes of single-crystal silicon carbide subjected to electrical discharge machining

CrossMark

Tsong-Han Tan [a], Jiwang Yan [b], *

[a] Graduate School of Integrated Design Engineering, Keio University, Yokohama, 223-8522, Japan
[b] Department of Mechanical Engineering, Keio University, Yokohama, 223-8522, Japan

ABSTRACT

Single-crystal silicon carbide (SiC) is an important semiconductor material used in power electronics. Due to its high hardness and brittleness, SiC is very difficult to machine using mechanical methods. Electrical discharge machining (EDM) has recently garnered extensive research interest as a potential machining method for SiC. However, this technique induces severe subsurface damage on the workpiece. To date, mechanisms leading to EDM-induced subsurface damage in SiC have not been clarified. This study aims to investigate the atomic-scale subsurface damage in SiC induced by EDM using Raman spectroscopy and transmission electron microscopy (TEM). In cross-sectional TEM observations, three regions of subsurface damage were identified, namely, the re-solidified layers, heat-affected zones, and microcracks. It was found that SiC decomposed into silicon and carbon in the re-solidified layers, and the degree of decomposition depended on the discharge energy and workpiece polarity. The re-solidified layer was a mixture of crystalline/amorphous silicon, crystalline/amorphous carbon, and nano-crystalline SiC. The presence of an extremely thin graphite layer was observed in the re-solidified layer. The heat-affected zone remained crystalline but showed a different crystal structure distinct from that of the bulk.

© 2016 Acta Materialia Inc. Published by Elsevier Ltd. All rights reserved.

1. Introduction

Single-crystal silicon carbide (SiC) is a hard and brittle material with high melting and boiling points. Due to its excellent physical, chemical, and electrical properties, such as high thermal stability, resistance to corrosion, and wide bandgap, SiC has become an important candidate material for applications exposed to high temperatures pressures, as well as corrosive environments. Owing to its wide bandgap, SiC also has the potential to replace silicon in high-power applications. The demand for SiC devices is predicted to rise rapidly in the near future. Ultraprecision machining of SiC is an essential step to ensure quality, reliability, and cost efficiency for SiC-based device manufacture, and is becoming increasingly important when the above technology trends are considered.

However, owing to its high hardness and brittleness, SiC is extremely difficult to machine using conventional methods such as mechanical polishing. On the other hand, SiC is electrically conductive, implying it can be finished by electrical machining methods. As a nonconventional machining technology, electrical discharge machining (EDM) has recently garnered research interest as a potential precision machining method for SiC. EDM does not involve mechanical contact between the tool and workpiece, and is therefore less affected by the workpiece hardness and brittleness.

Slicing of SiC ingots to produce thin wafers using wire-EDM (WEDM) has been an active area of research in recent decades. Kato et al. [1] compared the processes of WEDM slicing and diamond wire sawing of SiC ingots and concluded that WEDM achieved lower surface roughness but produced damaged layers containing SiO_2 and graphite. Yamamoto et al. [2] investigated the cutting of SiC ingots using a rotating WEDM slicing method and achieved a large kerf loss and improved surface roughness (3.4 μm Ra). Itokazu et al. [3] performed multi-wire EDM on a poly-crystalline SiC ingot and achieved satisfactory thickness variation. Yamamoto et al. [4] used a fluorine-based dielectric fluid in the WEDM of single-crystal SiC and concluded that improvement of surface roughness and kerf loss was achieved. Zhao et al. [5]

conducted EDM on single-crystal SiC ingots using a tensioned copper foil as an electrode for slicing, and concluded that this slicing technique performed better than the WEDM wafer slicing. Ishikawa et al. [6] compared the surface quality induced by fixed and loose abrasives wire cut with wire-EDM and found that the crystal lattice distortion produced by EDM was smaller than that by abrasives wire cut.

Despite the aforementioned advantages, a few problems still remain in the EDM of SiC. One is that EDM causes severe subsurface damage to SiC workpieces. A thick re-solidified layer and thermally induced microcracks will remain on the surface after EDM. Multiple subsequent polishing processes are required to remove the subsurface damage, but polishing is extremely time consuming. In light of this, understanding the subsurface damage and microstructural changes in SiC caused by EDM is essential for developing new processes for damage removal.

The main objective of this study is to investigate the subsurface damage induced by EDM. The emphasis is placed on characterization of the atomic-scale microstructural changes in SiC subjected to EDM. Elucidation of these microstructural changes will provide insights into the physics underlying the EDM of SiC, and enable process optimization for improving surface integrity.

Murray et al. [7] used transmission electron microscopy (TEM) and Raman spectroscopy to characterize the subsurface damage of single-crystal silicon caused by EDM, and found amorphous and crystalline silicon phases as well as subsurface cracks in the damaged layer. As single-crystal SiC has distinctly different material properties from silicon, the response of SiC to EDM might be different from that of silicon. However, to date, there has been no report in literature on the atomic-scale microstructural changes of SiC upon EDM. In the present study, TEM and Raman spectroscopy will be used to investigate the mechanisms causing atomic-scale subsurface damage to single-crystal SiC subjected to EDM.

2. Experimental procedures

2.1. Material

The workpiece used in this study was an *n*-type single-crystal 4H-SiC wafer with a surface plane of (0001). The wafer was 50 mm in diameter and 0.36 mm in thickness, with a chemo-mechanically polished finish. The 4H-SiC has a hexagonal structure with lattice constants of a = 3.073 Å and c = 10.053 Å. The main properties of the SiC workpiece are summarized in Table 1.

2.2. EDM setup and experimental conditions

EDM tests of single-crystal SiC were conducted on a RC-type EDM machine MG-ED72. As shown in Fig. 1, pulse generation of the RC-type EDM depends on the charging and discharging capacitors in the generator circuit. The EDM system uses a servo
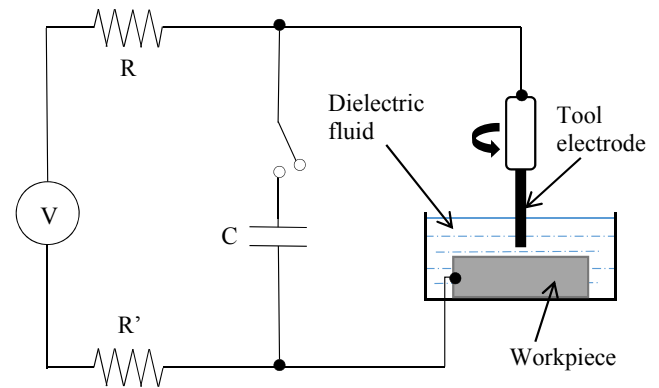

Fig. 1. Schematic diagram of the EDM experimental setup.

controlled machining system. The on-time/off-time of the electrical discharge pulse is controlled by the capacitor in the RC-circuit. A sintered polycrystalline diamond (PCD) rod (diameter 1.0 mm, diamond grain size 0.5 μm) was used as a tool electrode. As demonstrated by Yan and Tan [8], the PCD tool electrode has a very low wear rate and enables subsequent grinding after EDM for subsurface damage removal.

In this study, single-discharge and multiple-discharge machining tests were performed. Single discharge tests were performed to study the effect of discharge energy on crater generation by Raman spectroscopy, while multiple discharge tests were performed to create a sufficient surface area with a re-solidified layer for TEM analysis. In multiple discharge tests, grooves that were 1800 μm in length, 1000 μm in width, and 50 μm in depth were machined. The EDM conditions and the properties of the PCD electrodes are summarized in Table 2, and the corresponding discharged energy per pulse in Table 3.

2.3. Surface/subsurface characterization

Field emission scanning electron microscopy (FE-SEM, JEOL JSM-7600F) was used to observe the surface structures of the EDMed workpiece, and material compositions were characterized using an energy dispersive X-ray spectroscopy (EDS) system (Bruker AXS). A Taylor Hobson CCI type white-light interferometer with a 50 × objective lens was used to measure the surface topographies of the discharge-induced craters. The surface profile and crater depth were quantitatively measured with the assistance of the commercially available software TalyMap Platinum 6.2.

Laser micro-Raman spectroscopy was conducted at the centers of the electrical discharge induced micro-craters using a JASCO NRS-3100 Raman spectrometer to identify possible phase transformations in SiC. The excitation source used was a solid-state

Table 1
Properties of the SiC workpiece.

Property item	Value
Workpiece material	4H-SiC
Surface plane	(0 0 0 1)
Doping type	*n*-type
Electrical resistivity, [Ω·m]	$1.3-2.5 \times 10^{-4}$
Mohs hardness	~9
Thermal conductivity, [W/(m·K)]	370
Melting point, [°C]	2730
Sublimation temperature, [°C]	2830
Dielectric constant	9.76
Band gap, [eV]	3.26

Table 2
EDM conditions.

Parameter	Value
Input voltage, *V* [V]	70, 80, 90, 100, 110
Capacitance, *C* [pF]	3300
Polarity	Tool (+/−), Workpiece (−/+)
Tool electrode	Polycrystalline diamond (PCD)
Tool diameter, [mm]	1.0
Diamond grain size, [μm]	0.5
Binder (Co) concentration [%]	90
Electrical resistance, [Ω·m]	1.5×10^{-2}
Tool rotation rate [rev/min]	~3000
Dielectric fluid	Casty EDM oil

Table 3
Discharge energy per pulse with respect to input voltage.

Input voltage, V [V]	Discharge energy per pulse, E [µJ]
70	8.085
80	10.560
90	13.365
100	16.500
110	19.965

green laser with a 532 nm wavelength and a spot size of 1 µm. The laser exposure time for each measurement was 5 s, and each measurement was repeated 10 times. The laser output was controlled below 4.5 mW to prevent any thermal effects on the specimen.

In order to investigate the subsurface structure of the re-solidified layers on the EDMed surface, cross-sectional transmission electron microscopy (TEM) was performed using a FEI Tecnai G2 microscope at an acceleration voltage of 200 kV. For preparation of the samples, focused-ion beam (FIB) milling was performed using a FEI Quanta 3D filed emission gun (FEG), which has a gallium ion source, to produce a thin slice of the specimen (thickness ~100 nm). Before FIB operation, the surface was coated with osmium and platinum to prevent thermal damage to the specimen from the ion beam. The specimen was then cut perpendicularly to the EDMed surface (~10 µm in depth) by FIB milling. After the ion thinning process, the specimen was then lifted out by an in-situ micromanipulator on to the specimen holder for TEM observation.

3. Characterization of surface phenomena

3.1. Surface topography

Fig. 2 shows SEM micrographs of typical micro-craters on SiC induced by single discharge under different conditions. The topographies of the micro-craters vary with discharge energy and polarity. For each polarity, the size of the micro-crater increases when discharge energy increases. However, the crater size for positive workpiece polarity is larger than that for negative workpiece polarity even at the same discharge energy level. In addition, the micro-craters generated on a positive polarity workpiece appear to be smoother with a well-defined geometry. In contrast, the micro-craters generated on a negative polarity workpiece are rugged without a well-defined shape. The distinct differences in the appearance of the craters indicate different thermal erosion mechanisms.

As seen in Fig. 2, a common feature is that while a small portion of material has been vaporized and ejected from the micro-crater, a larger portion of material has melted and then re-solidified onto the top and fringe of the micro-crater. This is especially evident in Fig. 2(c), where a ring of pileup is formed around the crater, showing a significant degree of melting and flow. As shown in previous studies, the plasma temperature in a single electrical discharge can reach as high as 10000 K [9–11], which is far above the vaporization temperature of many materials, including SiC. Although some of the thermal energy dissipates into the surrounding dielectric fluid, generating both visible and invisible electromagnetic radiation [12], a large portion of the thermal energy is directed towards the workpiece and electrode. The intense thermal energy of the plasma channel from the electrical discharge vaporizes and melts the workpiece material.

Fig. 3 (a) shows a surface topography map of a micro-crater in which the height is depicted by color. The depth of the micro-crater can be obtained from the cross-sectional profile of the crater. Fig. 3

(b) presents the relation between crater depth and discharge energy. The error bars indicate the standard deviation of the crater depths measured for 25 single-discharge craters under each EDM condition. With increase in discharge energy, the depth of the craters increases for both workpiece polarities. The crater depth obtained for positive workpiece polarity is greater than that for negative workpiece polarity. The dependence of the crater depth on the workpiece polarity again demonstrates a difference in the thermal erosion mechanisms under the different conditions.

It is known from previous studies [13–15] that the size of the electrical discharge induced plasma near an anode is bigger than that near a cathode. A plasma channel is generated when electrons are emitted from a cathode. Since the mass of an electron is smaller than that of an ion by several orders of magnitude, electrons tend to travel and bombard the anode faster than ions. Therefore, the anode is heated and bombarded first by electrons, which are followed by negative ions travelling from the cathode, resulting in a larger and deeper crater cavity. In contrast, positive ions reach and heat up the cathode more slowly, and with a greater time delay, and thus result in a smaller and shallower crater cavity. In other words, the fraction of thermal energy transferred to the anode is larger when compared to the cathode.

3.2. Formation of silicon components

Many researchers [7,16–18] have reported that rapid melting/cooling of the workpiece material leads to formation of a re-solidified layer with different microstructures and phases. In this study, laser micro-Raman microscopy was performed on the re-solidified SiC surfaces inside the craters.

Fig. 4 shows Raman spectra of micro-craters in the range of $100–900$ cm^{-1} for various discharge energy levels and workpiece polarities. The as-received 4H-SiC (0001) shows distinctive Raman peaks at 774.4 cm^{-1} and 795.1 cm^{-1}, which is consistent with previous results by Nakashima and Harima [19]. After EDM, however, sharp peaks appear around 520 cm^{-1} at all discharge energy levels, indicating the formation of crystalline Si. The presence of Si indicates the decomposition of SiC into Si and C. As discharge energy increases from 8.085 µJ to 19.965 µJ, the intensity of the Si peak at 520 cm^{-1} shows a corresponding increase. This trend is similar for both workpiece polarities. For EDM with the workpiece at positive polarity (Fig. 4 (a)), the intensity of the 4H-SiC signature peak at 774.4 cm^{-1} decreases sharply as discharge energy increases, indicating a higher degree of SiC decomposition. For negative workpiece polarity, as shown in Fig. 4 (b), the signature Raman shift of 4H-SiC at 774.4 cm^{-1} remains evident throughout the discharge energy range. This suggests that 4H-SiC remains in the re-solidified layer even at high discharge energy.

The energy influx into a cathode workpiece (negative) is not as intense as to an anode workpiece (positive) even at the same level of discharge energy. The n-type 4H-SiC consists of free flowing electrons donated by the dopant, thus creating a resistive force in the workpiece against current flow from the cathode tool during electrical discharge. Such behavior is attributed to the diode-like rectifying phenomena in a semiconducting material [20]. Heat generation decreases due to such phenomena, with the result that correspondingly less SiC is decomposed in comparison with a cathode workpiece.

As discharge energy increases, together with the increase in Si peak intensity mentioned earlier, the peak at 520 cm^{-1} is also slightly broadened (Fig. 4). Broadening of a Si peak indicates the existence of nano-crystalline Si [21,22]. The existence of nano-crystalline Si was further confirmed by TEM studies of the re-solidified layer, as described in Section 4.

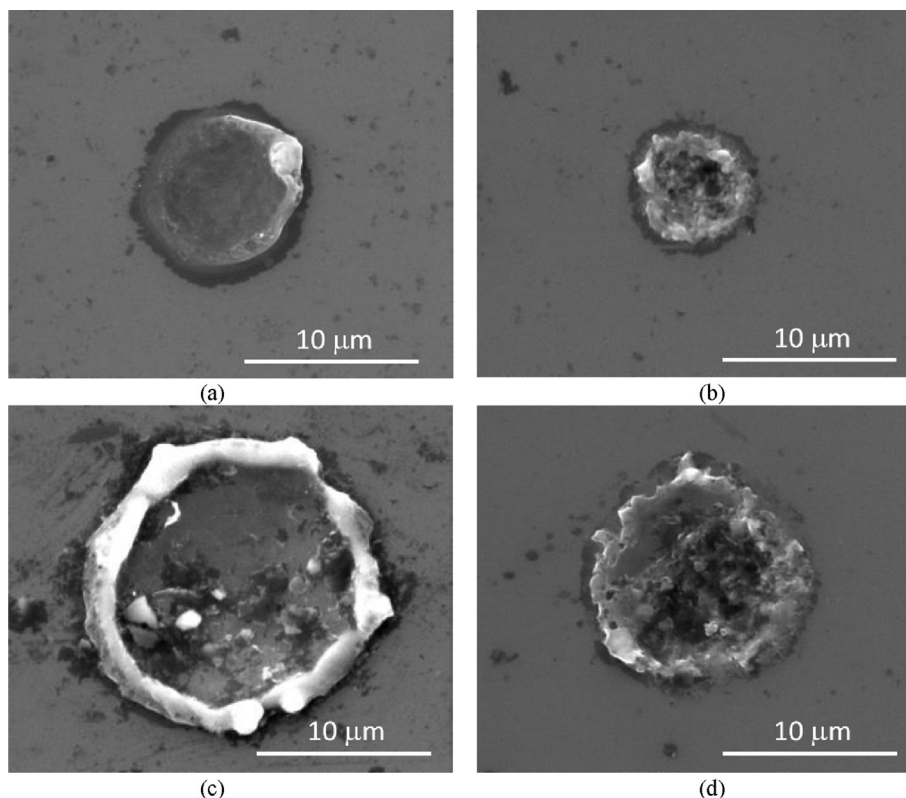We note that amorphous Si has also been identified via Raman

Fig. 2. SEM micrographs of micro-craters generated by single electrical discharges at various discharge energies and tool polarities: (a) workpiece positive, E = 8.085 µJ, (b) workpiece negative, E = 8.085 µJ, (c) workpiece positive, E = 19.965 µJ, (d) workpiece negative, E = 19.965 µJ.
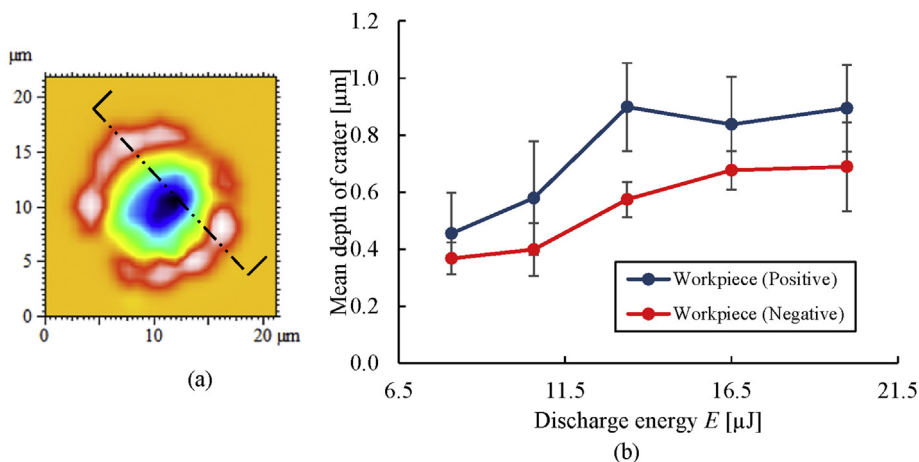

Fig. 3. (a) Surface topography of a micro-crater and (b) change of crater depth with discharge energy.

spectroscopy. Fig. 5 is a magnified view of a part of the Raman spectrum obtained at 19.965 µJ in Fig. 4 (b). A broad peak at around 470 cm^{-1} is clearly seen, which indicates the presence of amorphous Si [23,24]. The rapid cooling of the melt pool inside the micro-crater may lead to formation of an amorphous phase of Si in the outermost layer of the re-solidified surface, although crystalline Si remains the dominant phase that constitutes the re-solidified layer below the amorphous Si.

3.3. Formation of carbonaceous components

Fig. 6 shows the Raman spectrum in the 1100-1900 cm^{-1} range obtained from the re-solidified layers of the single-pulse discharge craters. In Fig. 6, a carbonaceous element is evident through the existence of D-band peaks at 1354 cm^{-1} and G-band peaks at 1590 cm^{-1}. The D- and G-bands are associated with vibrations of carbon in sp^2 and sp^3 bonding configurations. Specifically, the G-band is attributed to the stretching vibration in the basal plane of perfect graphite, while the D-band is associated with the breathing mode of the graphite structure, and indicates the presence of defects and disorder in the hexagonal sp^2 carbon structure [25–27]. The intensity ratio of D- and G-bands is often used as a measure of the degree of disorder in the graphitic structure [25,28], with increasing intensity ratio indicating increasing disorder of the graphite material.

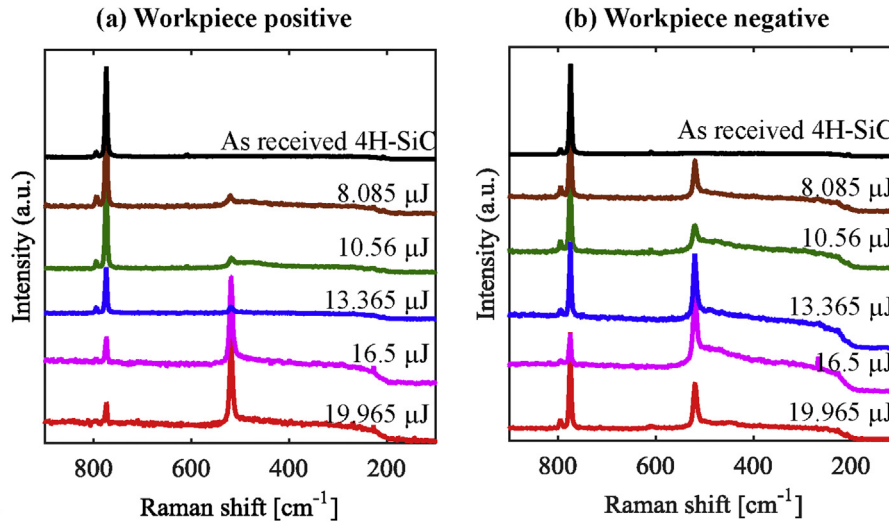In Fig. 6 (a), the D- and G-bands are not apparent at low

(a) Workpiece positive   **(b) Workpiece negative**

Fig. 4. Raman spectra of micro-craters formed by single discharge at various discharge energies using (a) positive and (b) negative workpiece polarity.
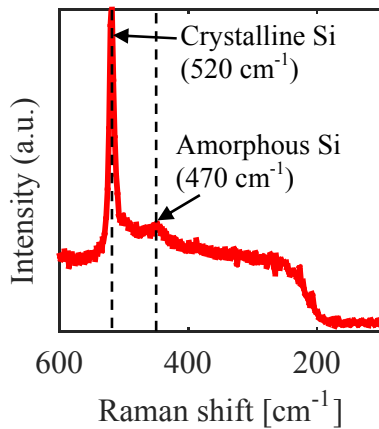

Fig. 5. Magnified Raman spectrum showing crystalline Si and amorphous Si in a micro-crater generated at 19.965 μJ using negative polarity.

discharge energy levels from 8.085 μJ to 13.365 μJ, but become very strong at discharge energy levels of 16.5 μJ and 19.965 μJ, and

resonate with the Si peaks detected under the same conditions (see Fig. 4 (a) in Section 3.2). This fact implies that when Si atoms dissociate from SiC molecules during thermal decomposition, C atoms form graphite crystallites in the re-solidified layer. TEM observations of this phenomenon will be presented in Section 4. When using negative workpiece polarity, as shown in Fig. 6 (b), very strong D- and G-bands are identified even at a very low discharge energy level (8.085 μJ). Furthermore, in contrast to positive workpiece polarity, discharge with negative workpiece polarity produces more carbon on the re-solidified layer.

It should be pointed out that apart from the carbon generated by the decomposition of SiC, some of the carbon detected on the re-solidified layer may also originate from vaporized hydrocarbon dielectric fluid and the PCD tool electrode. When the workpiece is set as the anode, its surface is charged positively, attracting negatively charged carbon ions to coalesce onto the surface. The heat in the discharge plasma not only vaporizes the hydrocarbon fluid, but also provides enough energy to ionize the molecule, thus producing negatively charged carbon ion species and positively charged hydrogen ions.
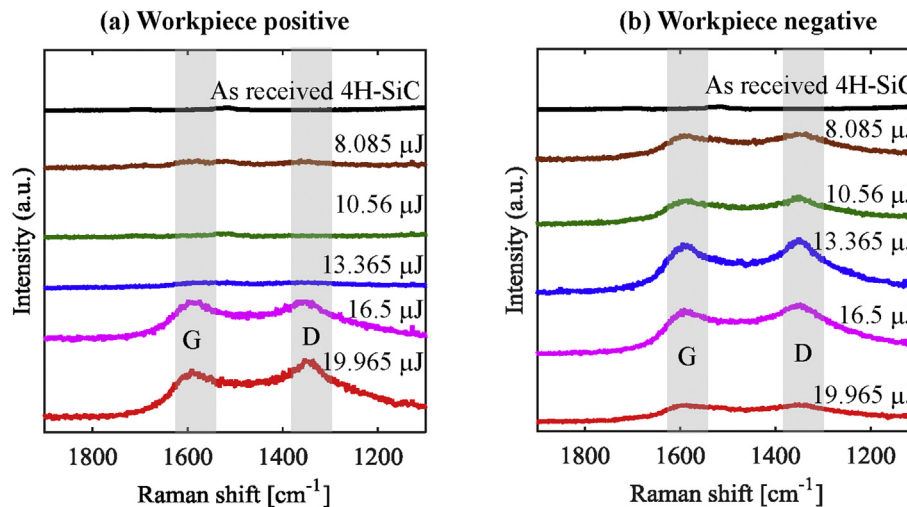
(a) Workpiece positive   **(b) Workpiece negative**

Fig. 6. Raman spectra indicating the formation of carbonaceous material on the surface of re-solidified layers in the micro-craters.

3.4. Debris formation

The phase diagram of the carbon-silicon binary system indicates that SiC with a 1:1 stoichiometric composition sublimes at 2830 °C into the gaseous state without going through a liquid phase [29,30]. When the vaporized SiC is cooled, it condenses into SiC particles. Fig. 7 shows the SEM images and EDS analysis of debris formed during EDM captured by filtering the dielectric fluid. The debris composition is SiC, verifying the above vaporization-condensation process of SiC.

The aforementioned Raman results and the EDS results strongly indicate the coexistence of vaporization and decomposition of SiC during EDM. As reported by previous studies, though SiC has strong covalent bonding, it begins to decompose at temperatures lower than the sublimation temperature [29,31]. In other words, at the thermal-erosion zone where the temperature is below its sublimation point, SiC decomposes into Si and C and re-coagulates as separate elements. The melting point of Si is lower (1414 °C), causing melting and material flow of the surface layer on a micro-crater (see Fig. 2(c) in Section 3.1).

4. Characterization of subsurface phenomena

4.1. Crack formation

A sample EDMed at 19.965 μJ per pulse (110V and 3300 pF) with negative workpiece polarity was used for conducting TEM observations. Fig. 8 (a) is a SEM micrograph of the sample after ion thinning and Fig. 8 (b) is the same sample lifted out by an in-situ micromanipulator and attached to a specimen holder and ready for TEM observation.

Fig. 9 shows TEM images of the sample. A subsurface crack (length ~1 μm) is observed beneath the re-solidified layer and heat-affected zone. Though EDM is a non-contact machining process, thermal effects play an important role in the formation of subsurface damage. Studies have shown that an electrical discharge generates an impulse force through the rapid expansion of the vapor of both the superheated material and the dielectric fluid [32,33]. Also, thermal stress arises due to steep temperature gradients generated on the surface during heating by plasma channels

and subsequent rapid cooling [34,35]. Formation of a crack is the result of a tensile stress exerted on the material that exceeds its fracture strength. The tensile stress might be induced by the different rates of heating/cooling between the re-solidified layer and the bulk material beneath it. In other words, the rapid expansion/contraction between the re-solidified layer and the bulk creates interfacial tensile stress and leads to initiation of crack formation.

4.2. Heat-affected zone

Fig. 10 (a) presents an enlarged view of the interface between the re-solidified layer and the unaffected bulk. A layer that is different from the bulk and the re-solidified layer is distinguished from its boundaries with both components. This layer is the heat-affected zone, where heat generated from the electrical discharges did not melt the material, but caused thermal effects. The thickness of the heat-affected zone measures approximately 150 nm. The selected area electron diffraction (SAED) pattern of the bulk shown in Fig. 10 (b) verifies the hexagonal lattice structure of 4H-SiC. The area of the heat-affected region is too small to perform SAED. Instead, the fast Fourier transform (FFT) image of the area is presented in Fig. 10 (c). The FFT image is a digital diffractogram similar to SAED, derived from the digitalized TEM image using the Gatan Micrograph software. The FFT result shows a crystalline structure, but the lattice structure is different from that of the unaffected 4H-SiC bulk. There are two possible reasons for the generation of the heat-affected layer: i) thermal strain or ii) the partial decomposition of SiC. The latter occurs when the temperature rises above 1600 °C but remains below the sublimation point of SiC (2830 °C), and leads to selective desorption of Si atoms from the SiC compound, leaving Si-rich and C-rich SiC phases, as demonstrated by Salama et al. [36]. Therefore, the heat-affected zone consists of alternating lamella of Si-rich and C-rich SiC phases, which appear as a banded structure in the bright field image.

4.3. Microstructure of the re-solidified layer

Fig. 11 presents a close-up TEM image of the re-solidified layer of the EDMed SiC sample. The re-solidified layer measures
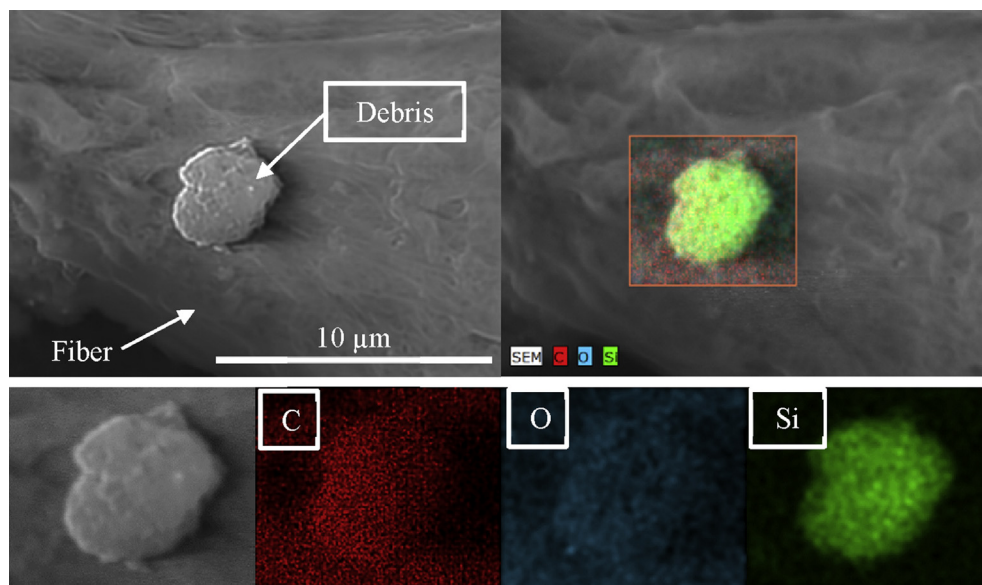

Fig. 7. SEM and EDS results of debris collected through filtering EDM oil.
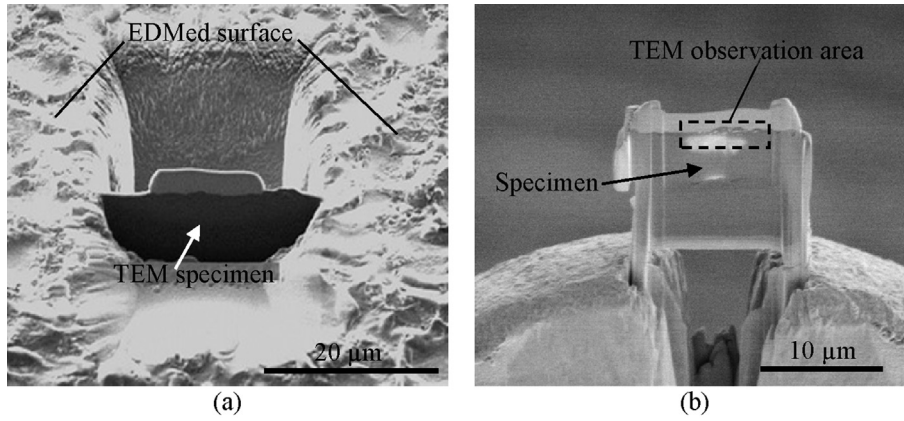
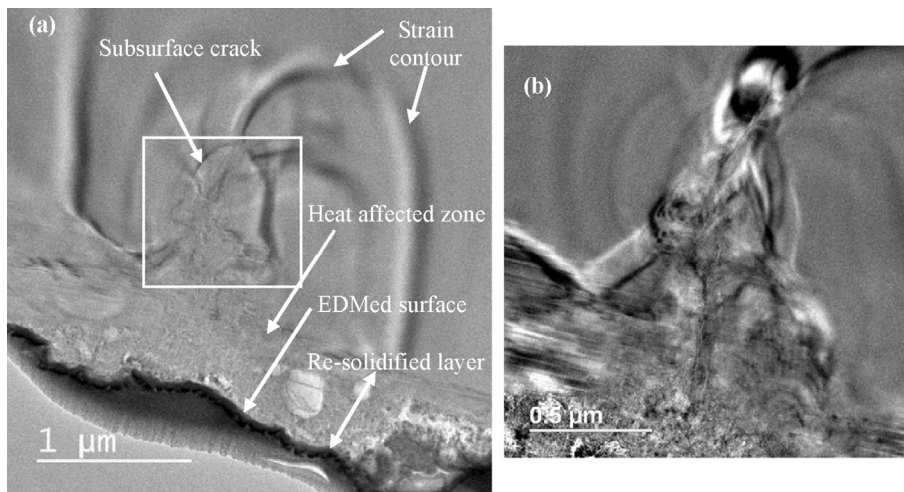**Fig. 8.** SEM micrographs of the FIB-thinned TEM specimen.

Fig. 9. (a) Bright field TEM image showing a subsurface crack beneath the re-solidified layer and heat-affected zone, (b) enlarged view of the region outlined by the square in (a).
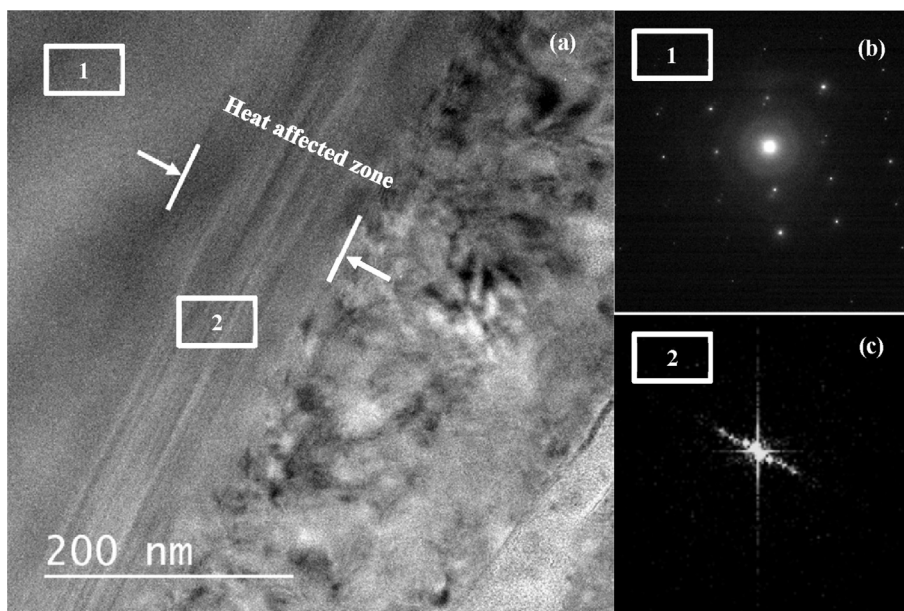

Fig. 10. The heat-affected zone at the interface of the re-solidified layer and unaffected bulk. (a) Bright field TEM image, (b) SAED of unaffected bulk, (c) FFT image of heat-affected zone.
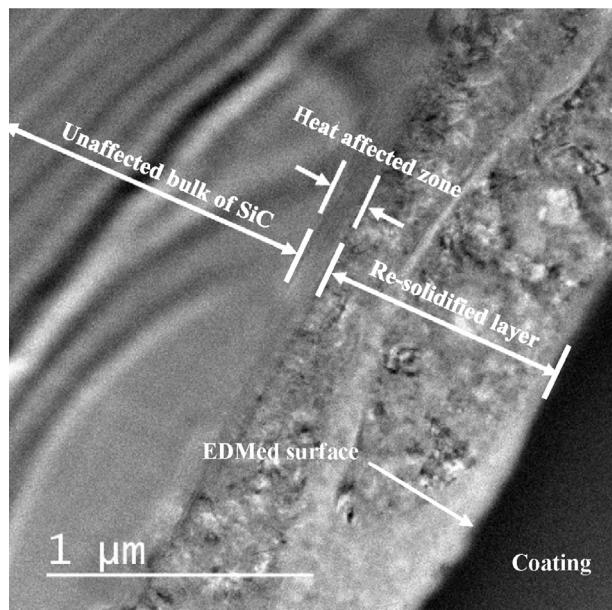
Fig. 11. Bright field TEM image of re-solidified layer on top of SiC bulk.

approximately 1 μm in thickness, and has an inhomogeneous microstructure with randomly distributed grains. The ripple-like contours observed in the bulk region in Fig. 11 might be due to bending of the TEM specimen.

Fig. 12 (a) presents a higher magnification TEM image of the re-solidified layer. Fig. 12 (b) is the FFT image of the entire area of Fig. 12 (a). The broad fringe-like diffraction pattern without any distinguishable bright spots indicates that an amorphous phase [37,38] exists in the selected region, which is approximately 500–600 nm deep into the EDMed surface. This agrees with the Raman spectroscopy result where peaks of amorphous Si (470 cm^{-1}) and amorphous carbon (1550 cm^{-1}) are detected (see Fig. 5 in Section 3.2 and Fig. 6 in Section 3.3). Despite the

dominating amorphous phase, the sparsely distributed bright spots in the FFT image of Region 2 in Fig. 12 (c) indicate the presence of a polycrystalline phase. In the bright field TEM image in Fig. 12 (a), nano-scale polycrystalline grains with distinguishable grain boundaries are visible.

4.4. Nanostructure of the silicon components

Fig. 13 presents a high-resolution TEM image of a small region inside the re-solidified layer. The TEM image in Fig. 13 (a) reveals the existence of different phases of material with observable boundaries. The FFT image in the inset shows a pattern of sporadic bright spots which indicates polycrystalline and amorphous phases. A crystalline Si phase can be identified with clear lattice fringes as seen in region 1 of Fig. 13 (a) and (c). Further confirmation is performed by analyzing the corresponding FFT image of region 1 as shown in Fig. 13 (b). The bright and distinctive spots shown in Fig. 13 (b) indicate a highly crystalline Si phase. However, upon closer examination, spots with weaker intensity can be observed in the background as well. This phenomenon may be attributed to crystalline grains with different orientations. By using analysis tools in the Gatan Microscopy software, the inter-planar spacing of the crystalline Si phase was measured as 0.324 nm. The measured value is close to that reported by Xu et al. [39] for crystalline Si with an *fcc* crystal structure (0.334 nm). Due to the solubility of carbon in the silicon matrix [40], the observed crystal lattices may contain trace amounts of the SiC structure. Such phenomena can cause the inter-planar lattice spacing to deviate from the theoretical value. However, in combination with the results from Raman spectroscopy, it can be concluded that crystalline Si exists as a major phase in the re-solidified layer.

4.5. Nanostructure of the carbonaceous components

Fig. 14 presents a high-resolution TEM image of a small region in close proximity to the bottom of the re-solidified layer and above the heat-affected layer. An embedded graphite layer is clearly seen, which consists of approximately 7–8 sheets in stacking sequence.
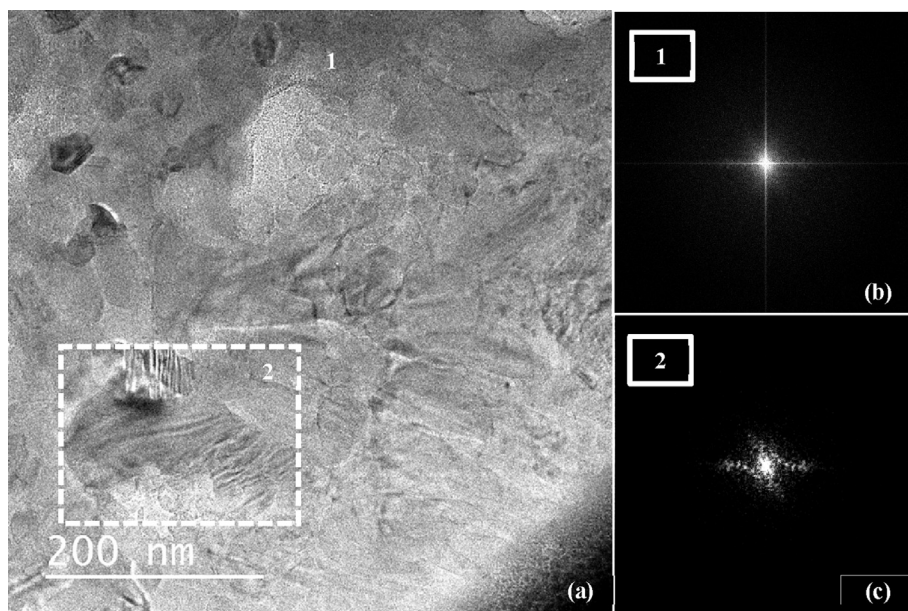

Fig. 12. (a) Bright field TEM image of the re-solidified layer; (b) FFT diffractogram of the entire region of (a), showing the amorphous phase; (c) FFT diffractogram of region 2 in (a), showing a polycrystalline microstructure.
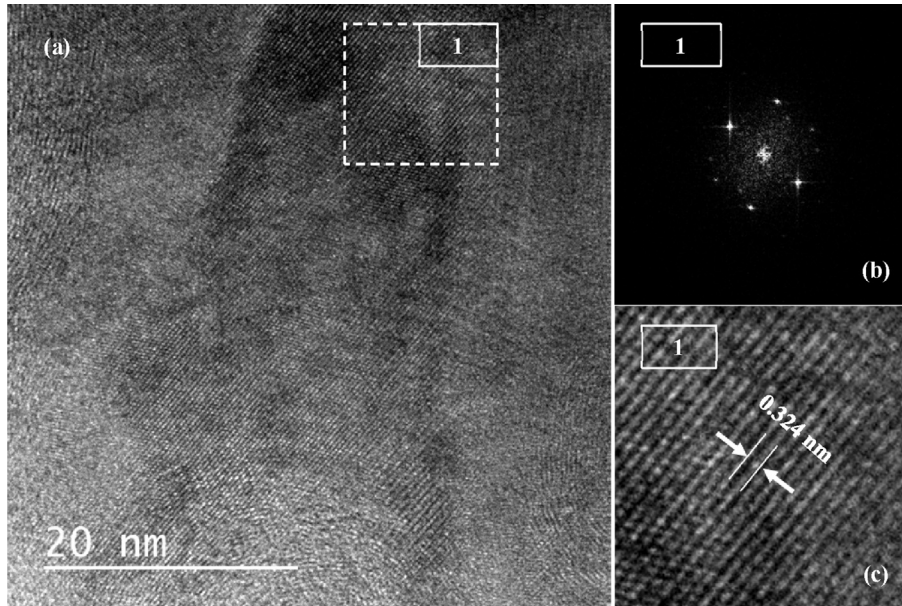
Fig. 13. Crystallization of silicon in the re-solidified layer. (a) Bright field TEM image of the re-solidified layer with different material phases. (b) Corresponding FFT image of region 1, (c) inter-planar spacing of crystalline Si.

The graphite layer is parallel to the workpiece surface, i.e., the (0001) plane, and the thickness of the graphite layer is measured to be about 3.2 nm, as indicated in region 2 of Fig. 14 (a). The FFT images in Fig. 14 (b), (c) and (d) are obtained from regions 1, 2 and 3 indicated in Fig. 14 (a). Region 1 mainly consists of polycrystalline SiC, while region 3 is mainly amorphous Si and C with a trace amount of polycrystalline SiC.

A further enlarged TEM image of the graphite layer is presented in Fig. 15 (a). Individual graphite sheets can be observed in a stacking structure, forming carbon ribbon bands. Analysis using inverse FFT and profile measurement techniques in the Gatan Micrography software, as shown in Fig. 15 (b) and (c) respectively, indicate that the inter-planar distance among the graphite sheets is 0.379 nm. This value is close to the inter-sheet spacing of an ideal hexagonal graphite structure [41,42]. However, the graphite layers are not perfectly aligned, and some disordered graphite sheets are
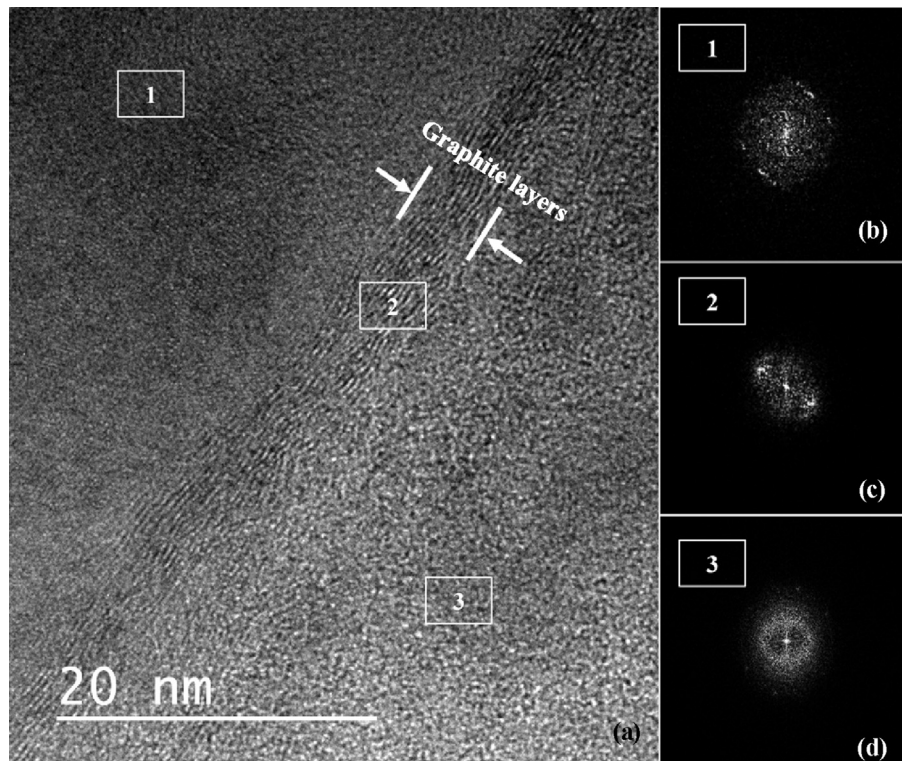

Fig. 14. High-resolution TEM images of the re-solidified layer, showing three regions: (1) polycrystalline SiC, (2) graphite layer, and (3) amorphous Si, C and nano-crystalline SiC.
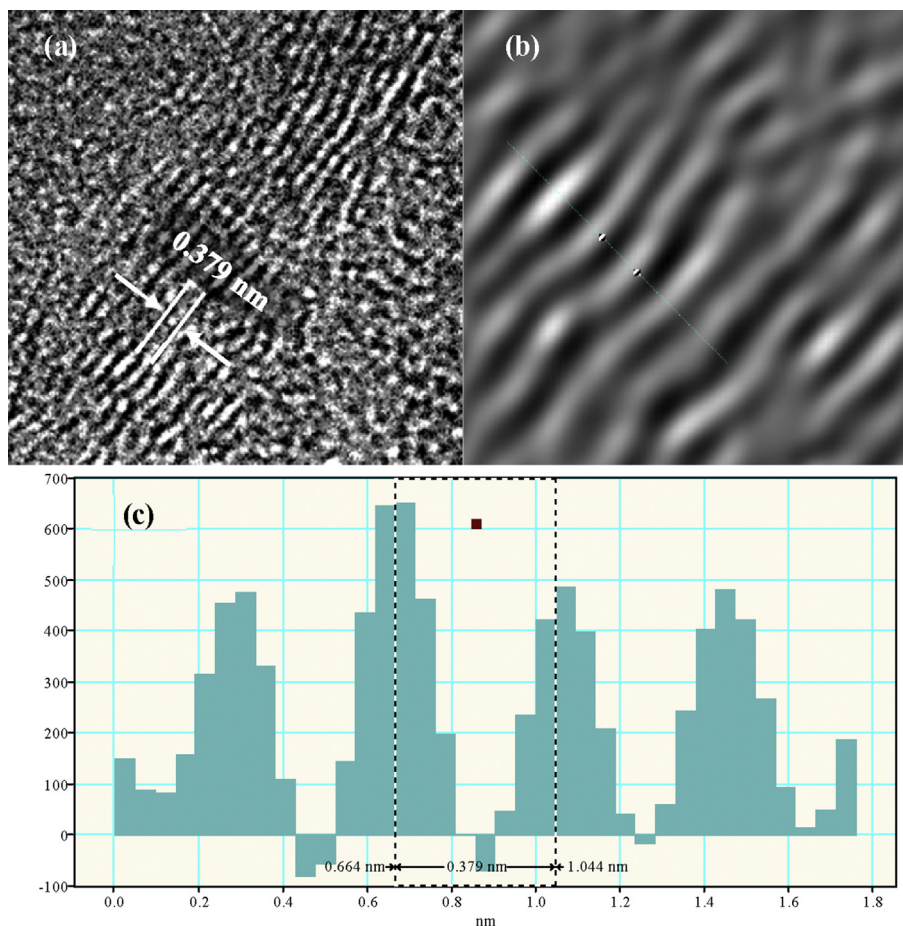
Fig. 15. Characterization results of the inter-planar distances of the multilayered graphite sheet: (a) Bright field TEM image, (b) inverse FFT image, (c) profile of inverse FFT.

present. This is in agreement with the Raman spectroscopy observation of the D-band, that signifies the existence of carbon with sp^3 bonding [25,28]. An ideal hexagonal graphite crystal only contains carbon atoms with sp^2 bonding without breathing mode.

Formation of the graphite layers might involve both thermal and mass transport of Si and C atoms during decomposition of SiC [36,43,44]. A combination of the temporal nature of the generated plasma channels, and the intense heating that occurs during electrical discharge means that the outer most surface of the workpiece experiences the highest temperature at the peak of discharge. Also, due to thermal conductivity of 4H-SiC, some of the thermal energy is transferred into the workpiece, forming temperature gradients and isotherm contours as the heat penetrates deeper. Temperature profiles and isotherm contours of discharge craters have been studied and modeled by many researchers [12,13,45,46].

Yeo et al. [45] presented simulated models of the thermal profile of a discharge crater in an AISI 4140 stainless steel workpiece that showed heat penetration up to 50 μm beneath the discharged surface. In 4H-SiC, the heat from electrical discharge is expected to penetrate even deeper, since the thermal conductivity of SiC is approximately seven times higher than that of steel at ambient temperature. Furthermore, the thermal conductivity of SiC is temperature dependent, increasing in value as temperature increases [47,48]. At temperatures above the boiling points of Si and C, which are 3625 °C and 3828 °C, respectively [29], both elements and their compounds exist in gaseous form. However, at temperatures between the peritectic point at 2830 °C [30] and the boiling point of silicon, Si atoms dissociate from C atoms and forms liquid silicon. This liquid dissolves small amounts of carbon. The remaining undissolved or saturated C atoms segregate and form graphite sheets in a stacking sequence.

A detailed examination of the graphite stacking in Fig. 15 (a) reveals imperfections of the graphite lattice, such as planar discontinuities or openings, stacking faults, and irregularities in parallel planes. Planar discontinuities might be attributed to the existence of vacancies on a planar hexagonal structure as a result of the amorphization of C atoms around the graphite sheet opening. Some graphite planes are observed to be bent and distorted. As the graphite layers are embedded in the polycrystalline/amorphous matrix, the graphite structures experience severe lattice strain due to inhomogeneity of multiple material phases. Rearrangement of carbon atoms to form graphite layers will also be disturbed by cyclic rapid heating and cooling during EDM. A similar phenomenon was reported by Salama et al. [36] in fabricating nanoribbons using nanosecond pulsed laser on 4H-SiC, where the inter-planar spacing of graphite layers was also 0.379 nm.

5. Conclusions

EDM tests of single-crystal 4H-SiC were performed under various conditions. Raman spectroscopy and TEM analysis were used to experimentally characterize the EDM-induced subsurface damages and structural changes in the material. The following conclusions were drawn:

(1) SiC is decomposed into silicon and carbon during EDM. The extent of decomposition depends on the electrical discharge

energy and workpiece polarity. Positive workpiece polarity causes greater decomposition of SiC.

(2) Though SiC does not melt directly in EDM, the decomposed silicon component undergoes melting and re-solidification, leading to a recast layer on the discharged crater surface.

(3) From the cross-section of an EDMed surface, three layers of subsurface damage can be identified: a re-solidified layer (thickness~1 μm), a heat-affected zone (thickness ~150 nm), and microcracks (length ~1 μm).

(4) Cracks are initiated beneath the re-solidified layer and heat-affected zone. The heat-affected zone remains crystalline but shows different crystal structures from that of the unaffected bulk.

(5) The re-solidified layer is a mixture of crystalline/amorphous silicon, crystalline/amorphous carbon, and nano-crystalline SiC.

(6) The crystalline phase of carbon in the re-solidified layer has a graphite structure and a thickness of several nanometers. The inter-planar distance among the graphite sheets is 0.379 nm.

References

[1] T. Kato, T. Noro, H. Takahashi, S. Yamaguchi, K. Arai, Characterization of electric discharge machining for silicon carbide single crystal, Mater. Sci. Forum. 600–603 (2009) 855–858.
[2] N. Yamamoto, S. Yamaguchi, T. Kato, Slicing of rotating SiC ingot by electric discharge machining, Mater. Sci. Forum. 740–742 (2013) 843–846.
[3] A. Itokazu, T. Hashimoto, K. Fukushima, T. Yuzawa, T. Sato, Multi-wire electrical discharge slicing for silicon carbide, Mater. Sci. Forum. 740–742 (2013) 841–842.
[4] N. Yamamoto, S. Yamaguchi, T. Kato, Effects of machining fluid on electric discharge machining of SiC ingot, Mater. Sci. Forum. 778–780 (2014) 767–770.
[5] Y. Zhao, M. Kunieda, K. Abe, Study of EDM cutting of single crystal silicon carbide, Precis. Eng. 38 (2014) 92–99.
[6] Y. Ishikawa, Y.-Z. Yao, Y. Sugawara, K. Sato, Y. Okamoto, N. Hayashi, et al., Comparison of slicing-induced damage in hexagonal SiC by wire sawing with loose abrasive, wire sawing with fixed abrasive, and electric discharge machining, Jpn. J. Appl. Phys. 53 (2014) 071301.
[7] J.W. Murray, M.W. Fay, M. Kunieda, A.T. Clare, TEM study on the electrical discharge machined surface of single-crystal silicon, J. Mater. Process. Technol. 213 (2013) 801–809.
[8] J. Yan, T.-H. Tan, Sintered diamond as a hybrid EDM and grinding tool for the micromachining of single-crystal SiC, CIRP Ann. - Manuf. Technol. 64 (2015) 221–224.
[9] K. Albinski, K. Musiol, A. Miernikiewicz, S. Labuz, M. Malota, The temperature of a plasma used in electrical discharge machining, Plasma Sources Sci. Technol. 5 (1996) 736–742.
[10] A. Kojima, W. Natsu, M. Kunieda, Spectroscopic measurement of arc plasma diameter in EDM, CIRP Ann. - Manuf. Technol. 57 (2008) 203–207.
[11] W. Natsu, S. Ojima, T. Kobayashi, M. Kunieda, Temperature distribution measurement in EDM arc plasma using spectroscopy, JSME Int. J. Ser. C 47 (2004) 384–390.
[12] A. Descoeudres, C. Hollenstein, R. Demellayer, G. Wälder, Optical emission spectroscopy of electrical discharge machining plasma, J. Phys. D. Appl. Phys. 37 (2004) 875–882.
[13] D.D. DiBitonto, P.T. Eubank, M.R. Patel, M.A. Barrufet, Theoretical models of the electrical discharge machining process. I. A simple cathode erosion model, J. Appl. Phys. 66 (1989) 4095.
[14] M.R. Patel, M.A. Barrufet, P.T. Eubank, D.D. DiBitonto, Theoretical models of the electrical discharge machining process. II. The anode erosion model, J. Appl. Phys. 66 (1989) 4104–4111.
[15] S.H. Yeo, W. Kurnia, P.C. Tan, Electro-thermal modelling of anode and cathode in micro-EDM, J. Phys. D. Appl. Phys. 40 (2007) 2513–2521.
[16] P.C. Pandey, S.T. Jilani, Plasma channel growth and the resolidified layer in edm, Precis. Eng. 8 (1986) 104–110.
[17] P.C. Tan, S.H. Yeo, Modeling of recast layer in micro-electrical discharge machining, J. Manuf. Sci. Eng. 132 (2010) 031001.
[18] Y. Zhang, Y. Liu, R. Ji, B. Cai, Study of the recast layer of a surface machined by sinking electrical discharge machining using water-in-oil emulsion as dielectric, Appl. Surf. Sci. 257 (2011) 5989–5997.
[19] S. Nakashima, H. Harima, Raman investigation of SiC polytypes, Phys. Status Solidi 162 (1997) 39–63.
[20] M. Kunieda, S. Ojima, Improvement of EDM efficiency of silicon single crystal through ohmic contact, Precis. Eng. 24 (2000) 185–190.
[21] C. Ossadnik, S. Veprěk, I. Gregora, Applicability of Raman scattering for the characterization of nanocrystalline silicon, Thin Solid Films 337 (1999) 148–151.
[22] G. Viera, S. Huet, L. Boufendi, Crystal size and temperature measurements in nanostructured silicon using Raman spectroscopy, J. Appl. Phys. 90 (2001) 4175.
[23] J. Smith, M. Brodsky, B. Crowder, M. Nathan, A. Pinczuk, Raman spectra of amorphous Si and related tetrahedrally bonded semiconductors, Phys. Rev. Lett. 26 (1971) 642–646.
[24] Z. Iqbal, S. Veprek, Raman scattering from hydrogenated microcrystalline and amorphous silicon, J. Phys. C Solid State Phys. 15 (1982) 377–392.
[25] A. Ferrari, J. Robertson, Interpretation of Raman spectra of disordered and amorphous carbon, Phys. Rev. B 61 (2000) 14095–14107.
[26] W. Lu, L.C. Feldman, Y. Song, S. Dhar, W.E. Collins, W.C. Mitchel, et al., Graphitic features on SiC surface following oxidation and etching using surface enhanced Raman spectroscopy, Appl. Phys. Lett. 85 (2004) 3495–3497.
[27] D.S. Knight, W.B. White, Characterization of diamond films by Raman spectroscopy, J. Mater. Res. 4 (1989) 385–393.
[28] A.C. Ferrari, J. Robertson, Raman spectroscopy of amorphous, nanostructured, diamond-like carbon, and nanodiamond, Philos. Trans. A. Math. Phys. Eng. Sci. 362 (2004) 2477–2512.
[29] R.W. Olesinski, G.J. Abbaschian, The C-Si (Carbon-Silicon) system, Bull. Alloy Phase Diagrams 5 (1984) 486–489.
[30] T. Kimoto, J.A. Cooper, Fundamentals of Silicon Carbide Technology: Growth, Characterization, Devices and Applications, John Wiley & Sons, Singapore, 2014.
[31] C. Faugeras, A. Nerrìre, M. Potemski, A. Mahmood, E. Dujardin, C. Berger, et al., Few-layer graphene on SiC, pyrolitic graphite, and graphene: a Raman scattering study, Appl. Phys. Lett. 92 (2008) 1–4.
[32] T. Tamura, Y. Kobayashi, Measurement of impulsive forces and crater formation in impulse discharge, J. Mater. Process. Technol. 149 (2004) 212–216.
[33] M. Tohi, T. Komatsu, M. Kunieda, Measurement of process reaction force in EDM using hopkinson bar method, J. Jpn. Soc. Precis. Eng. 68 (2002) 822–826.
[34] D.K. Panda, Study of thermal stresses induced surface damage under growing plasma channel in electro-discharge machining, J. Mater. Process. Technol. 202 (2008) 86–95.
[35] V. Yadav, V.K. Jain, P.M. Dixit, Thermal stresses due to electrical discharge machining, Int. J. Mach. Tools Manuf. 42 (2002) 877–888.
[36] I.A. Salama, N.R. Quick, A. Kar, Laser synthesis of carbon-rich SiC nanoribbons, J. Appl. Phys. 93 (2003) 9275.
[37] D.J.H. Cockayne, D.R. McKenzie, W. McBride, C. Goringe, D. McCulloch, Characterization of amorphous materials by electron diffraction and atomistic modeling, Microsc. Microanal. 6 (2000) 329–334.
[38] Z. Czigány, L. Hultman, Interpretation of electron diffraction patterns from amorphous and fullerene-like carbon allotropes, Ultramicroscopy 110 (2010) 815–819.
[39] B. Xu, X. Guo, Y. Ti, Universal Quantification of Chemical Bond Strength and its Application to Low Dimensional Materials, Graphene Simul., InTech, 2011.
[40] A.R. Bean, R.C. Newman, The solubility of carbon in pulled silicon crystals, J. Phys. Chem. Solids 32 (1971) 1211–1219.
[41] H.O. Pierson, Handbook of Carbon, Graphite, Diamonds and Fullerenes: Processing, Properties and Applications, William Andrew, 2012. https://books.google.com/books?id=Ub-GAAAAQBAJ&pgis=1 (accessed January 17, 2016).
[42] S. Welz, M.J. McNallan, Y. Gogotsi, Carbon structures in silicon carbide derived carbon, J. Mater. Process. Technol. 179 (2006) 11–22.
[43] W. Norimatsu, M. Kusunoki, Formation process of graphene on SiC (0001), Phys. E Low-Dimensional Syst. Nanostructures 42 (2010) 691–694.
[44] M. Kusunoki, T. Suzuki, T. Hirayama, N. Shibata, K. Kaneko, A formation mechanism of carbon nanotube films on SiC(0001), Appl. Phys. Lett. 77 (2000) 531–533.
[45] S.H. Yeo, W. Kurnia, P.C. Tan, Critical assessment and numerical comparison of electro-thermal models in EDM, J. Mater. Process. Technol. 203 (2008) 241–251.
[46] S. Tariq Jilani, P.C. Pandey, An analysis of surface erosion in electrical discharge machining, Wear 84 (1983) 275–284.
[47] E.A. Burgemeister, W. von Muench, E. Pettenpaul, Thermal conductivity and electrical properties of 6H silicon carbide, J. Appl. Phys. 50 (1979) 5790.
[48] R.P. Joshi, P.G. Neudeck, C. Fazi, Analysis of the temperature dependent thermal conductivity of silicon carbide for high temperature applications, J. Appl. Phys. 88 (2000) 265.